A General Framework for Change Detection Using Multimodal Remote Sensing Data

Sanid Chirakkal [ID], Francesca Bovolo [ID], *Senior Member, IEEE*, Arundhati Ray Misra,
Lorenzo Bruzzone [ID], *Fellow, IEEE*, and Avik Bhattacharya [ID], *Senior Member, IEEE*

Abstract—**A general framework for change detection is proposed to analyze multimodal remotely sensed data utilizing the Kronecker product between two data representations (vectors or matrices). The proposed method is sensor independent and provides comparable results to techniques that exist for specific sensors. The proposed fusion technique is a pixel-level approach that incorporates inputs from different modalities, rendering enriched multimodal data representation. Thus, the proposed hybridization procedure helps to assimilate multisensor information in a meaningful manner. A novel change index (ζ) is defined for the general multimodal case. This index is then used to quantify the change in bitemporal remotely sensed data. This article explores the usability, consistency, and robustness of the proposed multimodal fusion framework, including the change index, with proper validation on two multimodal cases: 1) the dual-frequency (C- and L-band) fully polarimetric Danish EMISAR data and 2) the dual-polarimetric synthetic aperture radar and Sentinel-2 multispectral data. Detailed analysis and validation using extensive ground-truth data are presented to establish the proposed framework.**

Index Terms—**Change detection (CD), dual-frequency PolSAR, Kronecker product of matrices, multimodal data, synthetic aperture radar (SAR) optical fusion.**

I. INTRODUCTION

IN 2009–2010, the Data Fusion Contest organized by the Data Fusion Technical Committee of the IEEE Geoscience and Remote Sensing Society focused its attention on detecting flooded areas using multitemporal and multimodal images. The performance of various approaches was evaluated based on Cohen's Kappa (κ) statistic. The best-ranked algorithm was the one that used data from both synthetic aperture radar (SAR) and optical sensors [1]. This outcome is indicative of a paradigm shift toward utilizing data from various sensors to perform decision fusion.

On the one hand, multitemporal remote sensing (RS) images from multiple sensors are becoming widely available, making it useful for researchers across various fields to develop change detection (CD) techniques catering to multimodal data [2], [3]. In contrast, a simple yet generic multimodal algorithm seems challenging due to varying changes of patterns inherent to different sensors and different spatial resolution [4].

While pixel-level multimodal fusion methods mainly focus on multispectral (MS) data fusion, high-level fusion includes feature-level and decision-level fusion of multisource data, such as SAR, MS, LiDAR, and other types of data [2]. Multimodal RS data have been integrated for land-cover CD [5] and classification of ecological zones [6]. A drought monitoring model has also been proposed using multisource RS data recently [7].

CD using single-mode RS data, such as MS image, is a mature area of research with techniques ranging from simple image differencing and rationing to advanced deep-learning-based ones [8]–[10]. Similar is the case with multitemporal SAR-based CD algorithms [11], [12].

Due to the increased availability of polarimetric SAR (PolSAR) data from various satellites, CD techniques on such datasets have also become vital to the RS community in recent years. CD using PolSAR images has been performed using hypothesis testing with a suitably defined test statistic on either the covariance ($\mathbf{C}$) or coherency ($\mathbf{T}$) matrices [13]–[16].

Beyond binary CD, the change vector analysis (CVA) or compressed CVA (C^2VA) has been used for multiclass CD [17], [18]. However, due to the speckle noise and the presence of complex scattering of electromagnetic waves from targets, the performance of CVA for SAR modality necessitates further assessment. A geodesic-distance-based approach between the Kennaugh matrices for a fully polarimetric (FP) SAR image for CD has been proposed in [19].

Although general fusion techniques have been well developed and widely applied for single modalities, they remain challenging for multisource data with varying spatial, spectral, and temporal characteristics. Multimodal data include, but are not limited to, dual-frequency PolSAR or SAR-MS images from sensors with different spectral channels and resolutions. Various techniques for the fusion of SAR-optical and subsequent CD algorithms have been reported in [20].

Quite a few among them show anomalies in the fused product while using conventional methods [21]. The grayscale difference is attributed to the significantly different imaging mechanisms of SAR and optical RS. Here, the SAR image is acquired as a high-resolution panchromatic image. Its spatial information is fused with the spectral information of the relatively low-resolution MS image. Fusion of SAR and MS images using Random Forest regression has also been recently proposed [22].

Meanwhile, a plethora of applications via fusion of SAR and optical images, such as annual crop inventories, urban land cover mapping, etc., are reported in the literature [23]–[27]. Bayesian statistical approaches to multimodal CD include works based on the Markov random field model [28] or fractal-projection- and Markovian-segmentation-based approaches [29]. Techniques based on the projection of multimodal data into a common feature space, on which one can apply well-known monomodal CD techniques, are also popular in the literature [30]–[32]. For multifrequency PolSAR data, the joint covariance-matrix-based techniques were introduced, which extends the CD techniques on single-frequency PolSAR data [33].

A framework for multiscale, multipolarization, and multifrequency SAR image preparation has also been introduced in recent times, which employs weighted-averaged Kennaugh elements (using Kennaugh matrices of individual frequencies) [34]. Fusion of P-band and L-band PolSAR and PolInSAR data for landcover classification has also been reported in [35].

Multimodal CD using direct learning from the training data has been reported in [36]–[39]. Furthermore, an unsupervised nonparametric method without requiring a training phase is proposed in [40]. Fusion of a hyperspectral image and data from multiple sensors, such as light detection and ranging, has been recently investigated with a convolutional neural network (CNN) framework [41]. Intending to provide land cover mapping through the fusion of multitemporal high-spatial-resolution and very-high-spatial-resolution satellite images, an end-to-end deep learning framework, M^3 fusion, was proposed in [42]. The dilemma of semisupervised transfer learning with limited cross-modality data in RS has been recently addressed using a deep learning framework, called X-ModalNet [43]. A general multimodal deep learning framework has also been proposed, which is not only limited to pixelwise classification tasks, but is also suitable to spatial information modeling with CNNs [44], [45].

This article proposes a generic and a simple framework for CD from multimodal data using the Kronecker product of feature vectors (or matrices) representing each data modality. This technique is sensor independent and requires no prior knowledge of the data distribution. A new change index (ζ) is defined, and detailed experiments demonstrate its usage. The proposed fusion technique is a pixel-level technique, which incorporates inputs from different modalities into single-resolution data, rendering enriched multimodal data representation.

The Kronecker product scheme adopted in our methodology is a robust mechanism to fuse information from various bands of multimodal data. The resulting representation is more practical and sensitive to changes due to the assimilation of information from two different modalities. This method is equally suitable for dual-frequency SAR data, where we utilize the Kennaugh matrix representation or vectors in MS images. Moreover, extension to more than two sources of information is relatively straightforward.

In this study, we provide a detailed analysis by demonstrating two experiments as examples of multimodal data. The first experiment uses multifrequency (C- and L-band) FP SAR data, while the second uses C-band dual-pol SAR and MS images. The wide range of applicability of the proposed framework emphasizes its universality. The hybridization of information from different sensors opens up new avenues for target identification, discrimination, and classification from remotely sensed data.

The contributions of this article are summarized as follows.
1) A pixel-level data fusion scheme is proposed for data from multiple sources, which uses a Kronecker product to combine information from individual modalities.
2) We propose a novel change index (ζ) with several desirable properties for binary CD.
3) We show the sensitivity of the derived ζ index under different change conditions, using statistical analysis of median and interquartile range (IQR).
4) We perform comparative analysis with state of the art for two experiments with multimodal RS data: a) dual-frequency PolSAR data and b) dual-pol SAR and MS data.
5) The proposed framework satisfies the need for a generic and pixel-level analysis that is simple to implement for multisource RS data fusion and CD. One should note that existing methods are either sensor specific or require learning techniques to achieve data fusion.

II. METHODOLOGY

Let t_1 and t_2 denote the prechange and postchange data acquisition instances, respectively. Let the single-modality remotely sensed data (for example, from SAR or MS sensors) be represented by $\mathbf{X}(t_k)$ and $\mathbf{Y}(t_k)$, for $k = 1, 2$. The prechange Kronecker product representation is denoted by $\mathbf{A}(t_1)$. In contrast, the postchange representation is denoted by $\mathbf{B}(t_2)$. The representation (i.e., matrix or vector) is mode (i.e., SAR or optical) dependent. Subsequent sections provide relevant examples of the proposed framework.

A. Change Index Using the Kronecker Product of Matrices

The pre- and postchange fused data representations of multimodal data, i.e., $\mathbf{A}(t_1)$ and $\mathbf{B}(t_2)$, are formed by using the Kronecker product of their single-modality representations, $\mathbf{X}$ and $\mathbf{Y}$ (we omit time information for simplicity). The Kronecker product of the two matrices, $\mathbf{X} = (x_{ij}) \in \mathbb{M}_{m \times n}$ and $\mathbf{Y} = (y_{ij}) \in \mathbb{M}_{p \times q}$, is denoted as $\mathbf{X} \otimes \mathbf{Y}$ and is defined as

$$\mathbf{X} \otimes \mathbf{Y} = \begin{bmatrix} x_{11}\mathbf{Y} & x_{12}\mathbf{Y} & \dots & x_{1q}\mathbf{Y} \\ \vdots & \vdots & \ddots & \vdots \\ x_{p1}\mathbf{Y} & x_{p2}\mathbf{Y} & \dots & x_{pq}\mathbf{Y} \end{bmatrix} \in \mathbb{M}_{mp \times nq}. \quad (1)$$

The matrix block $x_{ij}\mathbf{Y}$ is of the same dimension of $\mathbf{Y}$. The matrices $\mathbf{X}$ and $\mathbf{Y}$ are the original representations of the data

in their respective modalities. Some of the properties of the Kronecker product of two matrices are as follows [46].

1) Noncommutative, i.e., $\mathbf{X} \otimes \mathbf{Y} \neq \mathbf{Y} \otimes \mathbf{X}$.
2) Each entry of $\mathbf{X} \otimes \mathbf{Y}$ (or $\mathbf{Y} \otimes \mathbf{X}$) is of the form $x_{ij} b_{kl}$ (or $b_{kl} x_{ij}$).
3) $\mathbf{Y} \otimes \mathbf{X}$ can be obtained by permuting the entries of $\mathbf{X} \otimes \mathbf{Y}$, i.e., $\mathbf{Y} \otimes \mathbf{X} = \mathbf{P}(\mathbf{X} \otimes \mathbf{Y})\mathbf{Q}$, where $\mathbf{P}$ and $\mathbf{Q}$ are permutation matrices.

One can note that the noncommutative property of the Kronecker product distinguishes pseudogroups from groups.

Therefore, using the concept of the Kronecker product, we represent prechange information from multimodal sources at time t_1 as

$$\mathbf{A}(t_1) = \mathbf{X}(t_1) \otimes \mathbf{Y}(t_1). \tag{2}$$

The original representation (i.e., matrix or vector) of the multimodal data will vary according to the source of acquisition. Similarly, we represent postchange information from multimodal sources at time t_2 as

$$\mathbf{B}(t_2) = \mathbf{X}(t_2) \otimes \mathbf{Y}(t_2). \tag{3}$$

We propose a new change index (ζ) utilizing $\mathbf{A}(t_1)$ and $\mathbf{B}(t_2)$ as

$$\zeta(\mathbf{A}(t_1), \mathbf{B}(t_2)) = \frac{||\mathbf{A} - \mathbf{B}||_{\mathrm{F}}}{||\mathbf{A}||_{\mathrm{F}} + ||\mathbf{B}||_{\mathrm{F}}} \tag{4}$$

where $||\mathbf{A}||_{\mathrm{F}}$ is the Frobenius norm of the matrix defined as $||\mathbf{A}||_{\mathrm{F}} = \sqrt{\mathrm{Tr}(\mathbf{A}^{\dagger}\mathbf{A})}$, where Tr is the matrix trace (i.e., sum of the diagonal elements) and the superscript $\dagger$ denotes the matrix conjugate transpose. The following properties can be attributed to ζ.

1) $\zeta \in [0, 1]$.
2) High values of ζ indicate larger change between $\mathbf{A}$ and $\mathbf{B}$.
3) ζ is unitarily invariant.

We can perform change analysis using either simple thresholding techniques or CVA. The elements of the Kronecker product are considered individually before taking the norm for CVA. In contrast, one can apply thresholding techniques directly on the change index, ζ.

In this work, we performed change analysis using thresholding techniques. Global [47] or adaptive thresholding [48] techniques can be applied to ζ for binary CD. Adaptive thresholding considers the spatial variations in the neighborhood of each pixel to define a local threshold. The thresholded ζ image divides pixels into those belonging to change ω_c and no-change ω_{nc} classes. We present a flowchart of the complete fusion methodology in Fig. 1.

B. Case I: Dual-Frequency PolSAR Data

In FP SAR, the 2×2 complex scattering matrix $\mathbf{S}$ encompasses complete polarimetric information about backscattering from targets for each pixel. It is expressed in the backscatter alignment convention in the linear horizontal (H) and linear vertical (V) polarization basis as

$$\mathbf{S} = \begin{bmatrix} S_{\mathrm{HH}} & S_{\mathrm{HV}} \\ S_{\mathrm{VH}} & S_{\mathrm{VV}} \end{bmatrix} \Rightarrow \mathbf{k} = V([\mathbf{S}]) = \frac{1}{2}\mathrm{Tr}(\mathbf{S}\Psi) \tag{5}$$

where $\mathbf{k}$ is the scattering vector, $V(\cdot)$ is the vectorization operator on the scattering matrix, and Ψ is the corresponding basis matrix. Each element of the matrix represents the backscattering response of the target at a specific polarization. In the monostatic backscattering case, the reciprocity theorem constrains the scattering matrix to be symmetric, i.e., $S_{\mathrm{HV}} = S_{\mathrm{VH}}$.

The multilooked Hermitian positive-semidefinite 3×3 coherency matrix $\mathbf{T}$ is obtained from the averaged outer product of the target vector $\mathbf{k}_P$ (derived using the Pauli spin matrix basis set, Ψ_P) with its conjugate, i.e., $\mathbf{T} = \langle \mathbf{k}_P \mathbf{k}_P^{*T} \rangle$. Similarly, the 3×3 covariance matrix $\mathbf{C}$ is obtained from the averaged outer product of the target vector $\mathbf{k}_L$ (derived using the Lexicographic matrix basis set, Ψ_L) with its conjugate, i.e., $\mathbf{C} = \langle \mathbf{k}_L \mathbf{k}_L^{*T} \rangle$.

In this study, we utilize the 4×4 real matrix representation to describe backscattering in terms of the Kennaugh matrix $\mathbf{K}$. We can represent the Kennaugh matrix in terms of the elements of the $\mathbf{T}$ matrix as

$$\mathbf{K} =$$

$$\begin{bmatrix} \frac{T_{11}+T_{22}+T_{33}}{2} & \Re(T_{12}) & \Re(T_{13}) & \Im(T_{23}) \\ \Re(T_{12}) & \frac{T_{11}+T_{22}-T_{33}}{2} & \Re(T_{23}) & \Im(T_{13}) \\ \Re(T_{13}) & \Re(T_{23}) & \frac{T_{11}-T_{22}+T_{33}}{2} & -\Im(T_{12}) \\ \Im(T_{23}) & \Im(T_{13}) & -\Im(T_{12}) & \frac{-T_{11}+T_{22}+T_{33}}{2} \end{bmatrix} \tag{6}$$

where T_{ii} for $i = 1, 2, 3$ are the diagonal elements and T_{ij} for $i \neq j : i, j = 1, 2, 3$ are the off-diagonal elements of $\mathbf{T}$. $\Re$ and $\Im$ denote the real and imaginary parts of a complex number, respectively.

The Kennaugh matrix $\mathbf{K}$ provides a convenient representation of PolSAR data in terms of real quantities. The $\mathbf{K}$ matrix for two frequencies ($\mathbf{K}_{\nu_1}(t_1)$ and $\mathbf{K}_{\nu_2}(t_1)$) represents matrices $\mathbf{X}$ and $\mathbf{Y}$ defined in Section II-A, where ν_1 and ν_2 correspond to SAR acquisitions in two different frequencies (in this case L- and C-bands).

To compute the index, $\zeta(\mathbf{A}(t_1), \mathbf{B}(t_2))$, for analyzing change using dual-frequency PolSAR modality, we construct $\mathbf{A}(t_1)$ and $\mathbf{B}(t_2)$ as follows:

1) $\mathbf{A}(t_1) = \mathbf{K}_{\nu_1}(t_1) \otimes \mathbf{K}_{\nu_2}(t_1)$;
2) $\mathbf{B}(t_2) = \mathbf{K}_{\nu_1}(t_2) \otimes \mathbf{K}_{\nu_2}(t_2)$;

where the images are acquired by two frequencies ν_1 and ν_2 at time t_1 and similarly at time t_2. The Kronecker product of the two 4×4 Kennaugh matrices will produce a matrix of size 16×16 corresponding to the matrices $\mathbf{A}$ and $\mathbf{B}$.

C. Case II: Dual-Pol SAR and MS Data

For the fusion of dual-pol SAR and MS image, we considered four suitable bands from the MS images and the four elements of the Kennaugh matrix corresponding to the dual-pol SAR data [34]. The four elements of the $\mathbf{K}$ matrix can be written in terms of the elements of $\mathbf{C}_2$ matrix as

$$k_{11} = C_{11} + C_{22} \tag{7}$$

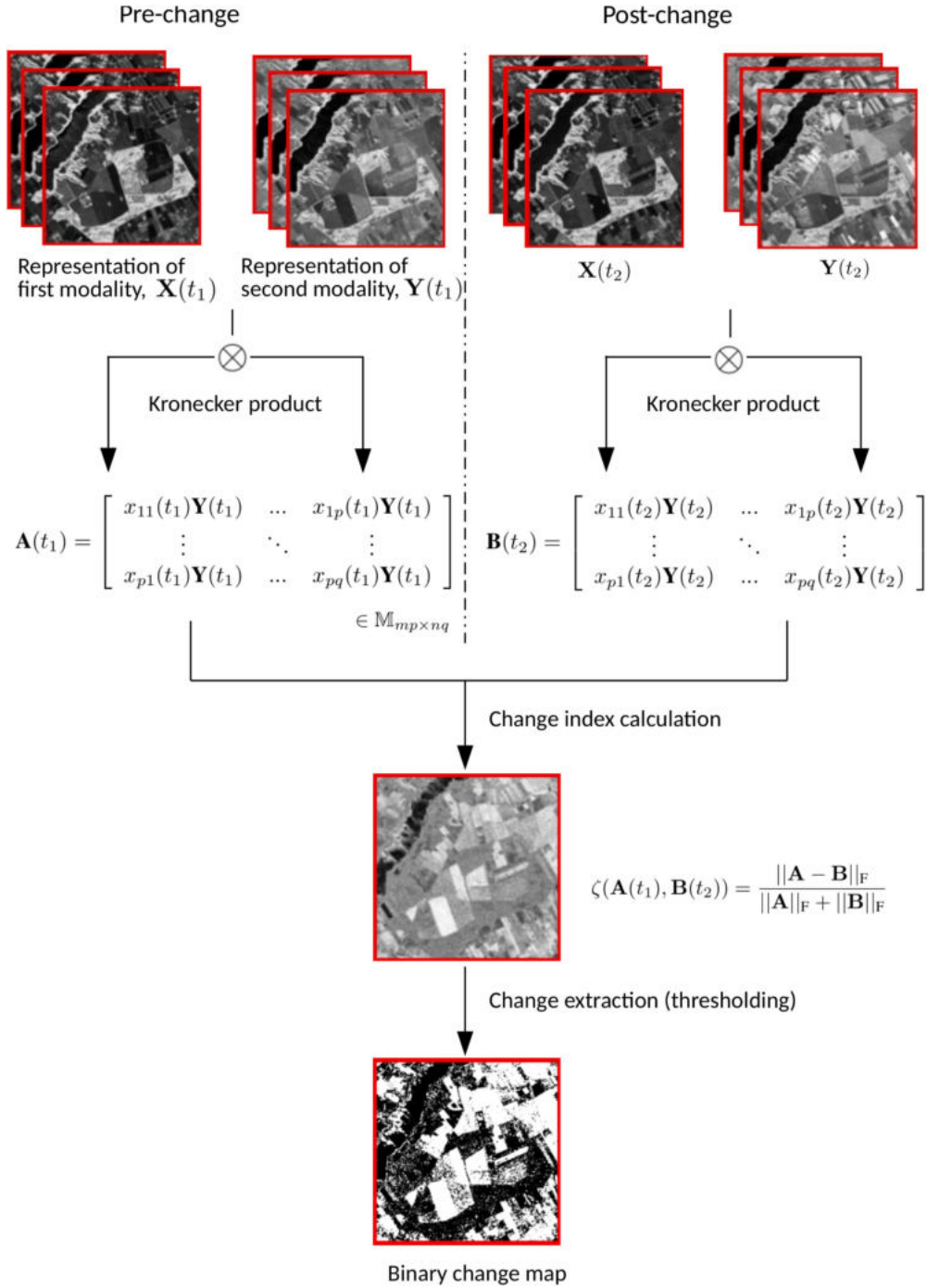$$k_{22} = C_{11} - C_{22} \tag{8}$$

$$k_{13} = \Re(C_{12}) \tag{9}$$

Fig. 1.   Graphical workflow for the proposed Kronecker product formalism. The images shown are for illustrative purpose only.

$$k_{24} = \pm \Im(C_{12}) \qquad (10)$$

where $\pm$ corresponds to the VV-VH and HH-HV modes, respectively.

We construct the prechange vector $\mathbf{A}(t_1)$ by using the Kronecker product of the vector for the MS bands $\mathbf{X}_{\mathrm{MS}}(t_1) = [x_1, x_2, x_3, x_4]^T$ and the vectorized Kennaugh matrix $\overline{\mathbf{K}}_\nu(t_1) =$

$[k_{11}, k_{22}, k_{13}, k_{24}]^T$ as

$$\mathbf{A}(t_1) = \begin{bmatrix} k_{11} \\ k_{22} \\ k_{13} \\ k_{24} \end{bmatrix} \otimes \begin{bmatrix} x_1 \\ x_2 \\ x_3 \\ x_4 \end{bmatrix} \qquad (11)$$

where ν is the frequency of the SAR data acquisition. Similarly, we can construct the postchange vector $\mathbf{B}(t_2)$.

Therefore, following (4), the change index, $\zeta(\mathbf{A}(t_1), \mathbf{B}(t_2))$ is defined for the fusion of dual-pol SAR and MS modality as
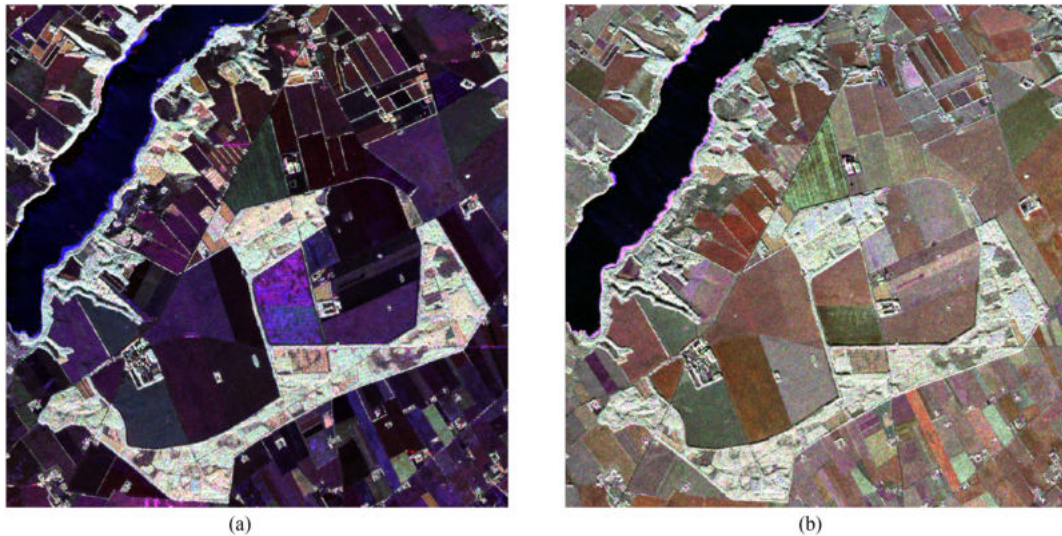
Fig. 2.   RGB color composite (using diagonal elements of the **C** matrix) of the Foulum agricultural study area. (a) *L*-band image of the EMISAR dataset for May 20, 1998. (b) *C*-band image of the same dataset.

1) $\mathbf{A}(t_1) = \overline{\mathbf{K}}_\nu(t_1) \otimes \mathbf{X}_{\mathrm{MS}}(t_1)$;
2) $\mathbf{B}(t_2) = \overline{\mathbf{K}}_\nu(t_2) \otimes \mathbf{X}_{\mathrm{MS}}(t_2)$.

In general, the selection of MS bands depends on the CD situation. For vegetated terrain, it is helpful to use the near-infrared (NIR) band (i.e., 770–895 nm). Vegetation reflectance in the NIR band and the indices derived from this spectrum range have been thoroughly investigated for plant canopies [49]. In this aspect, the normalized difference vegetation index is commonly used [50]. Therefore, we can use such indices to construct $\mathbf{X}_{\mathrm{MS}}$ preferably than the primary MS bands.

D. Change Index for Single-Modality Data

One can note that the definition of ζ, as in (4), is directly applicable for single-source data as well. We will use such an index to compare the output from the multimodal fused data to that from a single-channel data in Section IV. For single-source data, we have the native data representations in the form of $\mathbf{X}(t_1)$ and $\mathbf{X}(t_2)$ for the pre- and postchange acquisitions. We define ζ as follows:

$$\zeta(\mathbf{X}(t_1), \mathbf{X}(t_2)) = \frac{||\mathbf{X}(t_1) - \mathbf{X}(t_2)||_{\mathrm{F}}}{||\mathbf{X}(t_1)||_{\mathrm{F}} + ||\mathbf{X}(t_2)||_{\mathrm{F}}}. \qquad (12)$$

III. DATASETS, STUDY AREA, AND GROUND TRUTH

A. Experiment I: Dual-Frequency PolSAR Data

We demonstrate the dual-frequency case utilizing the FP multifrequency Danish airborne EMISAR data. The EMISAR system operates at two frequencies: *C*-band at 5.3 GHz (5.7-cm wavelength) and *L*-band at 1.25 GHz (24-cm wavelength) [51]. The spatial resolution of the nominal one-look image is 2m × 2m (one-look) with a ground range swath of approximately 12 km. The processed data are fully calibrated by using an advanced internal calibration system. For this study, we used the *L*- and *C*-band data simultaneously acquired on March 21,

May 20, June 16, and July 15, 1998. All acquisitions were coregistered by identifying ground control points in the images and using an interferometric DEM acquired by the EMISAR system. Before resampling, we transformed the original one-look scattering matrix data to the covariance matrix representation. These data were averaged to reduce the speckle by a cosine-squared weighted 9 × 9 filter. The new pixel spacing in the images is 5m × 5m, and the effective spatial resolution is approximately 8m × 8m at mid-range.

The study area is located at the Foulum Research Centre of the Danish Institute of Agricultural Sciences, Jutland, Denmark. The test site contains many agricultural fields with different crops, lakes, forests, natural vegetation, grasslands, and urban areas. The area is relatively flat, and the local incidence angle corrections due to terrain slope are redundant. Spring crop types include beets, peas, potatoes, maize, spring barley, and oats. Winter crops include rye, winter barley, winter wheat, winter rape, and grass. An RGB color composite (using diagonal elements of the covariance matrix of each frequency) of the study area is given in Fig. 2, where (a) is the study area imaged in the *L*-band and (b) is the study area imaged in the *C*-band for May 20, 1998.[1]

For each acquisition date, a land cover map was provided, including more than 350 test areas. The individual development stage of crops is described by the BBCH decimal scale ranging from 0 to 99. The first digit is the main development stage. The second digit is a subdivision of the main stage, e.g., for cereal crops, 0–9 corresponds to germination, 10–19 to leaf development (the second digit is the number of leaves unfolded), 20–29 to tillering (the second digit is the number of tillers detectable), 30–39 to stem elongation, 40–49 to booting, 50–59

---

[1]The EMISAR data are available to scientific partners and, to a limited extent, for customers. (One should contact Prof. Erik Lintz Christensen for further information on costs and availability.)

TABLE I
GROUND TRUTH OF SELECTED CROP FIELDS FOR THE FOULUM IMAGE OF 1998 FOR MAY, JUNE, AND JULY

Field id	Crop	Height April	BBCH April	Height May	BBCH May	Height June	BBCH June	Height July	BBCH July
1	Winter wheat	14	29	42	39	78	58	90	81
2	Peas	n/a	n/a	12	14	42	52	69	71
3	Rye	n/a	22	55	63	94	61	88	82
4	Spring oats	n/a	n/a	22	29	66	43	99	69

We consider only a small subset of the fields in this work. Note that data for some dates were not available.

to heading, 60–69 to flowering, 70–79 to development of fruit, 80–89 to ripening, and 90–99 to senescence. Similar definitions are available for other crops. For a detailed description of the ground-truth (GT) data, refer to [13]. The details of the four fields mentioned in this work are given in Table I. One can observe that over the considered period, as expected for agricultural crops, the change is continuous and pervasive. Under this condition, the proposed change index is validated in terms of sensibility to the change (see Section IV-A) rather than on the binary CD map quality.

B. Experiment II: Dual-Pol SAR and MS Data

We demonstrate this case by using Sentinel-1 SAR and Sentinel-2 MS Instrument bands. The Sentinel constellation data are freely available from the Copernicus open access hub. Further preprocessing is required for the SAR-MS fusion as compared to dual-frequency SAR (the flowchart shown in Fig. 3). We considered the Junagadh district of Gujarat, Western India, as the study area. Here, groundnut is widely cultivated, along with cotton being the only major competing crop. The district has a tropical wet and dry climate with three seasons: mild winter, hot summer, and monsoon. In the summer months, the temperature ranges between 28 and 38 °C, while in winter, it ranges between 10 and 25 °C with an average annual rainfall of 827 mm. Usually, the sowing of groundnut starts with the onset of the monsoon. But where irrigation facilities are available, premonsoon sowing is arranged during the last week of May or during the first week of June with presowing irrigation, which increases the yield.

We conducted a field survey in August 2019 to collect GT samples of groundnut and cotton fields. An app-based approach was adopted, allowing polygons to be specified, often covering the whole field over the required area. Traditional methods usually take a single latitude/longitude point measurement using a handheld GPS. Collecting GT based on polygons can offset any error in GPS readings, while also allowing the collection of samples from inaccessible areas. As many fields are protected using fencing, this method improves the number and quality of GT samples. Fig. 4(a) and (b) shows photographs of a typical groundnut field and cotton field, respectively, taken during the field survey. We collected 32 polygons of groundnut and 21 polygons of cotton during the survey.

We make use of the bitemporal Sentinel-1 and Sentinel-2 (L2A product) images. For MS bands, we use Sentinel-2's MS imager, blue (B2 at 490 nm), green (B3 at 560 nm), red (B4 at
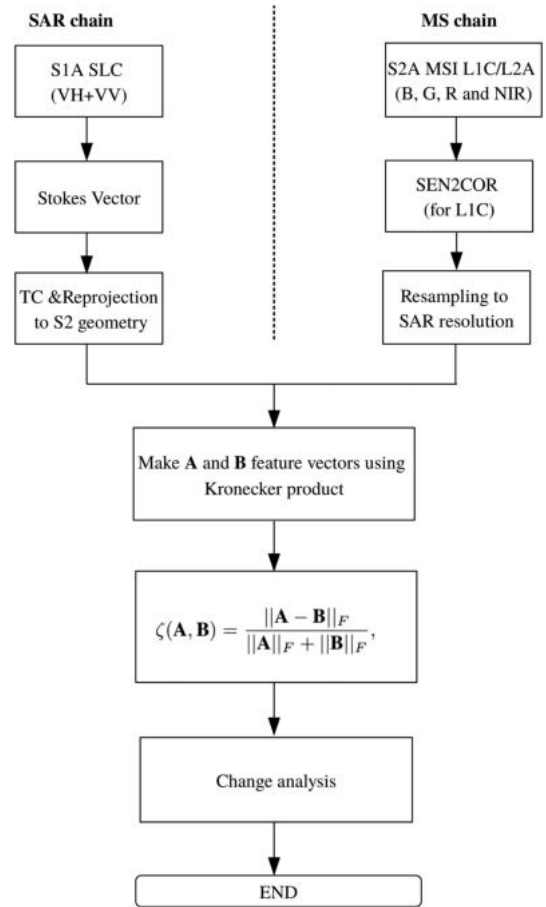

Fig. 3. Workflow shows the proposed framework for the specific case of SAR-MS fusion. As compared to the standard workflow described in Fig. 1, there are additional preprocessing steps.

665 nm), and NIR (B8 at 842 nm) bands, all at 10-m resolution. So, the feature vector $\mathbf{X}_{\text{MS}}$ defined in Section II-C would be for Sentinel-2 data as

$$\mathbf{X}_{\text{MS}} = \begin{bmatrix} B_2 \\ B_3 \\ B_4 \\ B_8 \end{bmatrix}. \tag{13}$$

Apart from the primary color bands, we considered the NIR band at 842 nm because of the agricultural study area, and thus, the B8 band is sensitive to vegetation. Preprocessing involves

Fig. 4. (a) Photograph of a typical groundnut field taken during the field survey in August 2019. (b) Photograph of a typical cotton field.

TABLE II
SPECIFICATIONS OF DUAL-POL SENTINEL-1 INTERFEROMETRIC WIDE SWATH (IW) MODE DATA USED FOR THE STUDY

Property	Value
Satellite	Sentinel 1A
Sensor type	SAR
Acquisition type	IW mode (SLC)
Study area	Junagadh, Gujarat
Acquisition dates	02-April-2019 11-October-2019
Polarization	Dual Pol (VH and VV)
Pass	Descending
Sample Type	Complex
Azimuth spacing (m)	13.97
Range spacing (m)	2.33
Center Lat/Lon.	20.646°/70.780°
Radar frequency (GHz)	5.4

converting L1C to L2A (if required), resampling to SAR resolution, and reprojection to a common projected geometry (see Fig. 3 for details). The L1C products provide "the top of atmosphere" reflectance in fixed cartographic geometry, whereas L2A products provide the "bottom of atmosphere" reflectance in the same geometry.

The bitemporal Sentinel-2 L2A data used in this study are on April 6 and October 8, 2019, which are close to the SAR acquisition dates. The details of the SAR data are given in Table II. Like Dataset I, we observe that change is prevalent in a crop area considering acquisition dates with a long time gap. Accordingly, the proposed change index will be validated in terms of its sensitivity to the change (see Section IV-A) rather than its performance for binary CD.

IV. RESULTS AND DISCUSSIONS

A. Experiment I: Dual-Frequency SAR Modality

In this section, we demonstrate the sensitivity of the novel ζ index to various kinds of changes in the Foulum agricultural fields. As mentioned, the Foulum study area is an agricultural site, where most of the pixels belong to the change class (ω_c). Thus, the sensitivity is evaluated using the statistical variables of median and IQR. This analysis is performed in a multidate setup computing ζ between every subsequent couple of images. This allows studying the behavior of ζ under varying change conditions as the crops evolve toward their phenological season. As an example of the possible outcome of the detection step, binary change maps for one couple of dates are provided for qualitative comparison.

The change index, ζ, for the dual-frequency (L- and C-bands) EMISAR data via the proposed method is demonstrated in Fig. 5(a). The change index shown in the figure is between March and May 1998 acquisitions over the agricultural site. We compared the results with CD techniques tailored explicitly for the multitemporal PolSAR data proposed by Nielsen *et al.* [33].

The PolSAR covariance matrices are Wishart distributed, which generalizes the gamma distribution to multiple dimensions. The multifrequency covariance matrices also follow Wishart distribution if constructed directly from the six-component Lexicographic target vector. But even in cases where they are built out of $\mathbf{C}$ matrices of individual frequencies as block-diagonal matrices, it is possible to derive the same formula for the test statistic as in the case of the full multifrequency covariance matrix. The test statistic "$-\ln Q$" is defined as [33]

$$\ln Q = n(2p \ln 2 + \ln |\mathbf{A}| + \ln |\mathbf{B}| - 2 \ln |\mathbf{A} + \mathbf{B}|) \quad (14)$$

where $\mathbf{A}$ and $\mathbf{B}$ are the 6×6 joint covariance matrices (block-diagonal) of the dual-frequency PolSAR data for the pre- and postchange dates, $p = 6$ for our case, n is the number of looks, and $|\mathbf{A}|$ is the determinant of $\mathbf{A}$. The probability of finding a value smaller than the observed value (z), $P(-2\rho \ln Q < z)$, can also be derived, which involves calls to incomplete gamma
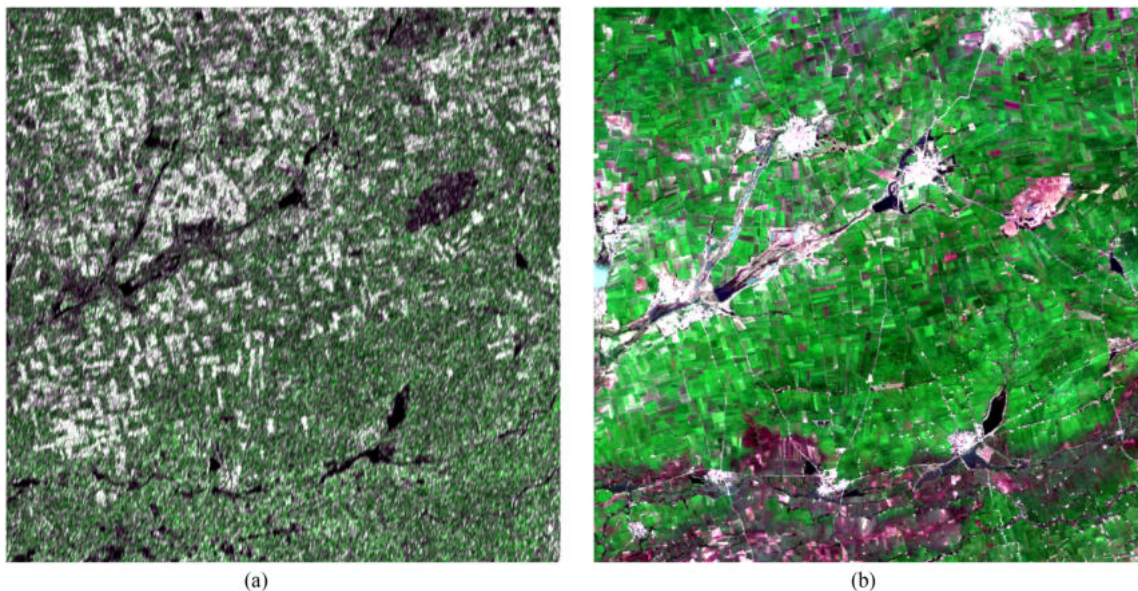
Fig. 5. Groundnut and cotton fields of the Junagadh district of Gujarat state in India are imaged by Sentinel-1 and Sentinel-2 satellites. (a) RGB representation (pseudocolor composite) of the first and second elements of the Kennaugh feature vector for the dual-pol Sentinel-1 A SAR image on October 11, 2019. The third band is a reinsertion of the first band. (b) Natural color composite of the Sentinel-2B satellite image was acquired on October 8, 2019. The bands are B_2, B_3, and B_4, respectively, for the RGB bands. The field boundaries are well delineated in the MS image, whereas the dual-pol SAR image reveals other characteristics.

function ($\rho = 0.8910$) [33]. The probabilities are then thresholded to make a change map.

The comparison of ζ with the test statistic, $-\ln Q$, is given in Fig. 5(a) and (b). One should note that the test statistic, unlike ζ, is not normalized between 0 and 1. Both change indexes show brighter areas (higher values) as the change intensity increases. Apart from the difference in dynamic range, it is clear from Fig. 5(a) and (b) that both the methods can capture changes associated with crop growth. The probability of observing a value less than $-2\rho \ln Q$ is calculated for the test statistic, and we prepare a change map by thresholding probability at 0.9999. To detect changes in ζ, we have used an adaptive thresholding technique. The binary change images are shown for qualitative analysis in Fig. 6(a) and (b) for ζ and the test statistic, respectively. ζ shows more changes in the waterbody as compared to the test statistic in these figures.

It is interesting to note that some changes are appropriately captured by the proposed method (such as the field marked as "1" in Fig. 5), whereas they are less evident using the test statistic. The opposite is true for other fields, such as the one marked "2" in the same figure. We can analyze the sensitivity of the change index to the growth stages of the crops to gain more insight. For this, the change index (and the test statistic) is calculated between pairs of acquisitions for March–May, May/June, and June/July, corresponding to the dates "d1," "d2," and "d3" on the x-axis of the Fig. 7. The field marked "1" in Fig. 5 is a winter wheat field that starts at 14-cm height (BBCH—29) in April and grows to 90 cm by July (BBCH—81).

In May, the field records an average height of 39 cm (BBCH—78), while it was 78 cm (BBCH—58) in June. This growth is recorded better with ζ compared to the test statistic, as can be seen in Fig. 7(a) and (b). Note that we calculated the change

indices among each subsequent couple of dates and not w.r.t the start date. Hence, once the growth speed reduces relative to the first pair of dates, the corresponding value of ζ drops (despite growth between dates). Also, the index captures the changing intensity and not its direction; thus, growth and decay reflect similarly in it. The red lines mark the median values and the box edges for the first and third quartile (thus giving the IQR). While both parameters record a similar trend of progressive saturation (as the crop achieves the phenological peak), the sensitivity is more in the ζ parameter than in the statistic. The separability of the ω_c (here the winter wheat) and ω_{nc} classes are better in the new index as compared to the test statistic (14). This is conspicuous in Fig. 7(a) and (b) boxplots. The gray plots are for ω_{nc} (here a waterbody marked "W" in Fig. 5), which gives the baseline median values when there is little or no change between acquisitions (0.21, 0.20, and 0.18 for the three pair of acquisitions as given in Table III). The blue plots are for ω_c and show relatively high ζ values (compared to ω_{nc} baseline ones) for all the dates. The difference between ω_c and ω_{nc} is less pronounced in $-\ln Q$.

For the peas field marked "2," the changes are captured better in the test statistic [see Fig. 7(c) and (d)]. The peas field has an average height of 12 cm in May (BBCH—14), 42 cm in June (BBCH—52), and 69 cm in July (BBCH—71). Again, both the indexes show a very similar trend, but the test statistic shows higher sensitivity to change. The median values of ζ are all close together (0.37, 0.41, and 0.37), while the values of $-\ln Q$ are scattered (see Table III). The lack of change for the peas field is clear from the binary change map (see Fig. 6) too. The histograms of ζ for these two fields of interest are shown in Fig. 8. The peak of the peas field histogram is shifted toward lower values than the winter wheat, again confirming the earlier
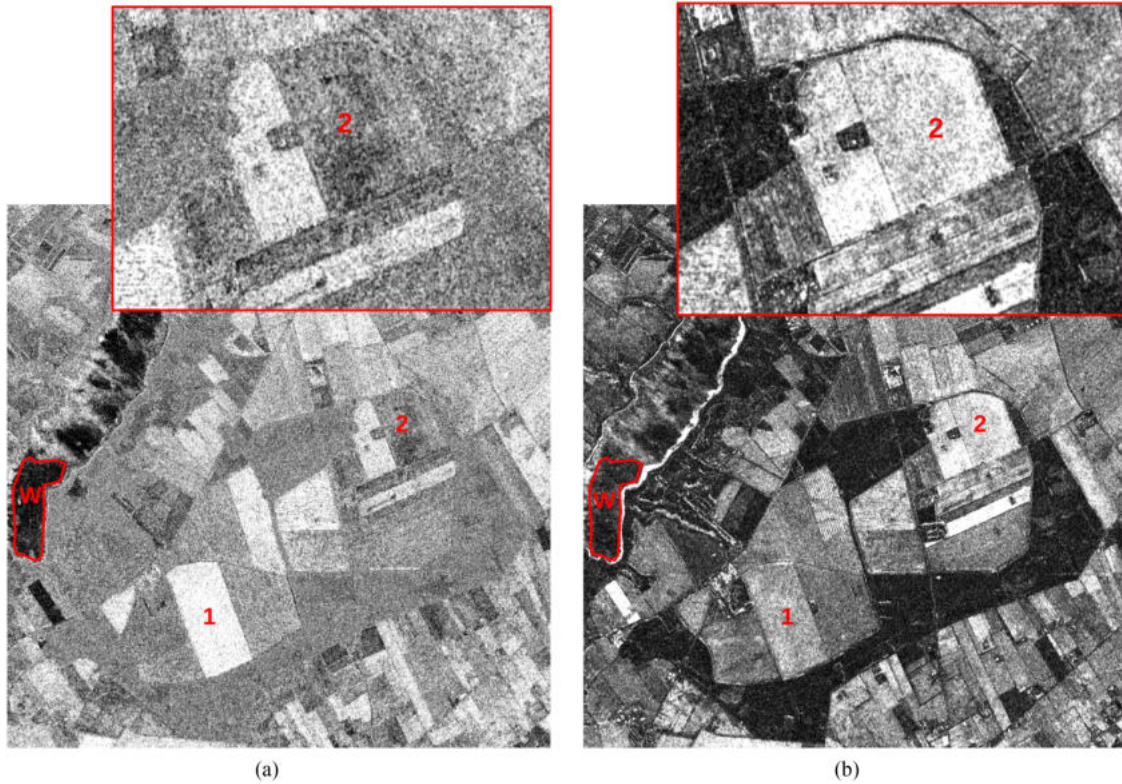
Fig. 6. Inferring change from the dual-frequency EMISAR data over the Foulum agricultural fields in Denmark for March and May 1998 images. (a) Normalized change index (ζ) using both L- and C-bands. (b) Test statistic, $-\ln Q$, as proposed in [52] for CD on dual-frequency PolSAR data. (Inset) Zoomed-in portion for the Peas field marked "2." "W" is representative of the "no-change" class (ω_{nc}), here depicting a waterbody.
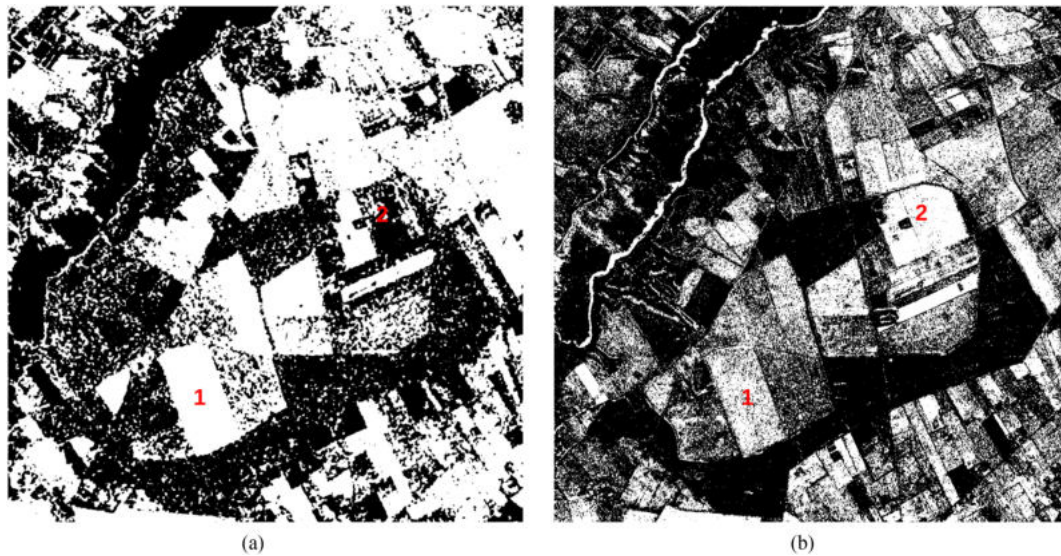

Fig. 7. (a) ζ image thresholded using adaptive method based on local statistics. (b) $P(-2\rho \ln Q \leq z)$ between March and May 1998 thresholded at 0.9999. In binary change map, white pixels are labeled "change," whereas black pixels are labeled "no change."

observations. However, interestingly, the separability w.r.t the ω_{nc} baseline is still consistent, for all dates, in the proposed formalism [see Fig. 7(c) and (d)]. Again, this is not true for the test statistic, where the separability is very poor for the last pair of acquisitions (d3).

It is also worth seeing the advantages of hybridizing the information in L and C channels compared to using them individually. It is known that L- and C-bands have different responses to different crops, which is expected given their different wavelengths [53], [54]. Fig. 9(a) and (b) depicts normalized

TABLE III
MEDIAN AND IQR OF VARIOUS CHANGE INDICES FOR THE WINTER WHEAT AND PEAS FIELDS

| Class	Index	Date-1		Date-2		Date-3	
		Median	IQR	Median	IQR	Median	IQR
Winter wheat	$-\ln Q$	34.10	9.84	22.53	8.55	16.81	6.69
	ζ	0.56	0.06	0.45	0.08	0.31	0.09
	ζ_L	0.46	0.08	0.38	0.09	0.17	0.08
	ζ_C	0.42	0.09	0.25	0.10	0.26	0.10
Peas	$-\ln Q$	42.95	10.85	52.89	12.96	20.92	7.39
	ζ	0.37	0.10	0.41	0.09	0.37	0.09
	ζ_L	0.25	0.10	0.34	0.10	0.28	0.11
	ζ_C	0.27	0.10	0.24	0.09	0.26	0.09
Waterbody	$-\ln Q$	14.67	6.75	10.79	5.82	16.11	7.94
	ζ	0.21	0.08	0.20	0.08	0.18	0.07
	ζ_L	0.12	0.06	0.10	0.06	0.11	0.06
	ζ_C	0.17	0.08	0.16	0.08	0.13	0.07
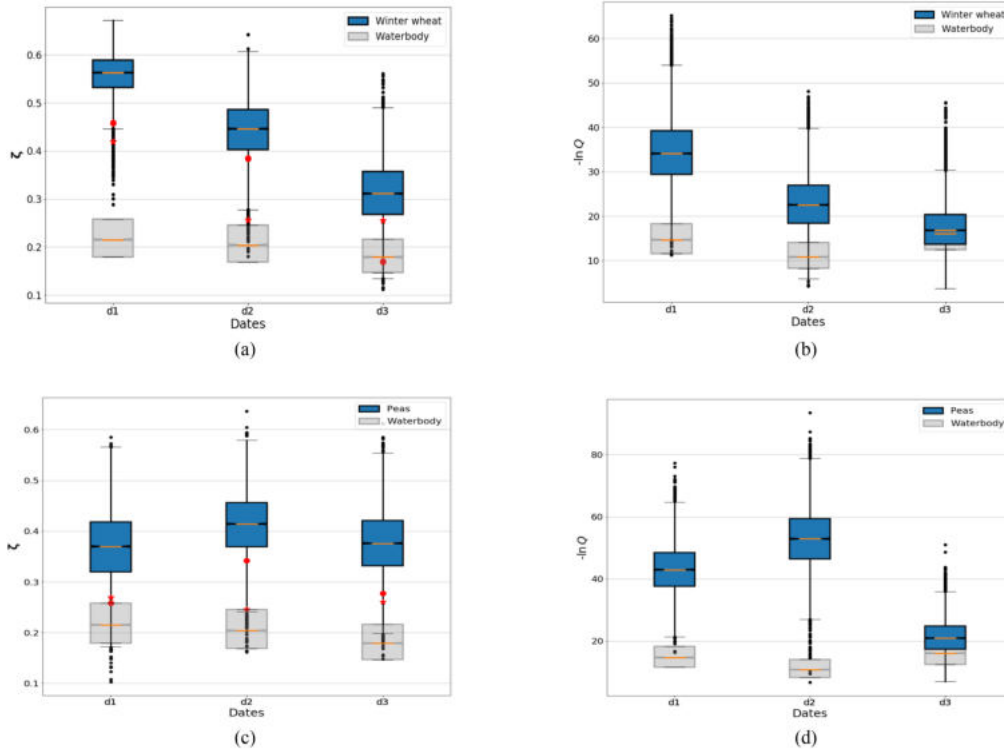
Fig. 8.	Box and whisker plot of the change indices for the winter wheat field marked "1" and the peas field marked "2." The change indices are calculated between March–May, May–June, and June–July. (a) and (c) ζ parameter for winter wheat and peas, respectively, for the aforementioned dates. The dots and asterisks are the median values of ζ only using the L- or C-band. (b) and (e) Test statistic, $-\ln Q$, for winter wheat and peas for the same dates. The gray boxplots (without whiskers and outliers) are for the waterbody class (as depicted in Fig. 5) representative of the no-change (ω_{nc}) class.

change index using bitemporal L- and C-band only, respectively, over the Foulum agricultural fields. We make use of (12) here to derive the single channel ζ.

It is evident that, while changes in agricultural fields are captured better in the L-band, specific changes in the waterbody are adequately reflected in the C-band. This also provides better

flood monitoring of vegetated areas with an integrated L- and C-band approach [55]. In the C-band, many agricultural fields report hardly any growth at all, as evidenced by missing bright areas in Fig. 9(b). However, an average of these two behaviors is observed in the fused ζ image, as depicted in Fig. 5(a). An exception to this rule cab is noticed in the field labeled by id
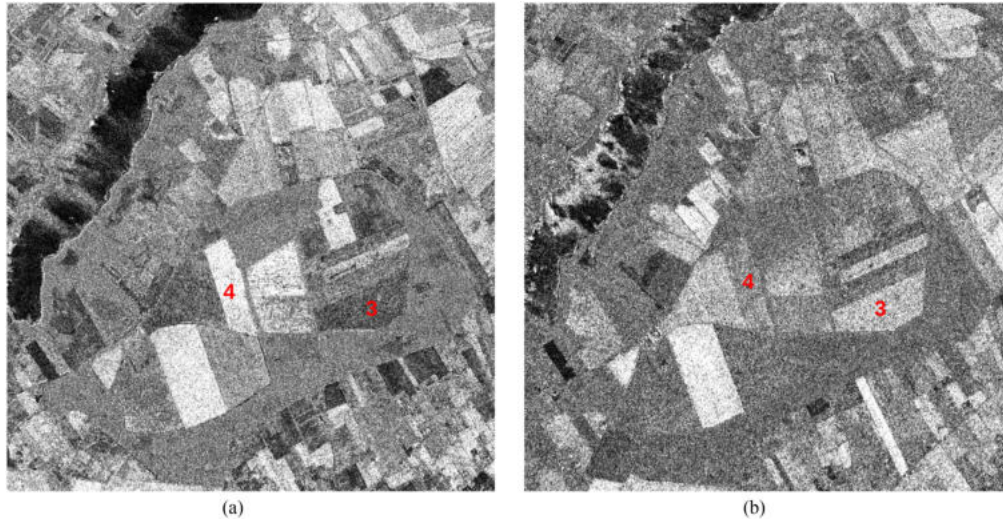
Fig. 9. Normalized change index using (a) L-band (ζ_L) and (b) C-band (ζ_C) only.

"3," a Rye field. This crop changes from BBCH 22 to 88 by July. Irrespective of this growth, the difference in ζ_L using the L-band alone is much less than that using only C-band (ζ_C). See Table III for the comparison of the magnitude of change index. Recall that lighter tones indicate more change and darker tones indicate less change in ζ images. Rye field has a darker shade in the L-band as compared to the lighter shade in the C-band [see Fig. 5(a) and (b)]. Interestingly, an average of these two behaviors is observed in the new change index, which is of moderate light shade.

The opposite behavior is observed for the fields labeled "4" (spring oats). Here, the change in the L-band is considerable, while the C-band registers much less change. ζ from the fusion product again reflects the combined effect of both these frequencies.

Furthermore, the change index defined via the Kronecker product formalism captures the growth of the crops with reasonable sensitivity, whereas the changes captured in either frequency alone are less. In Fig. 5(a) and (c), the median values of the L- and C-bands are depicted as dot and asterisks, respectively. The L-band performs relatively better in capturing changes in agricultural fields than the C-band, which saturates quite quickly. This is to be expected due to the shorter wavelength of the C-band as compared to the L-band. The median values and the IQR of various change indices (both multimodal and single modality) are summarized in Table III.

As our methodology does not involve any learning-based approaches, the process takes short computational time. For the 1024×1024 tiles used in the dual-frequency PolSAR fusion, the entire process finishes within 4 min in the python3 framework on a workstation with 64-GB RAM and Intel Xeon processor. We obtain 256 elements by vectorizing the Kronecker product, which provides us with C(256,2) combinations for the CVA. This in itself is a robust area of research, and many techniques of dimensionality reduction can be applied here, including C ^{2} VA [18].
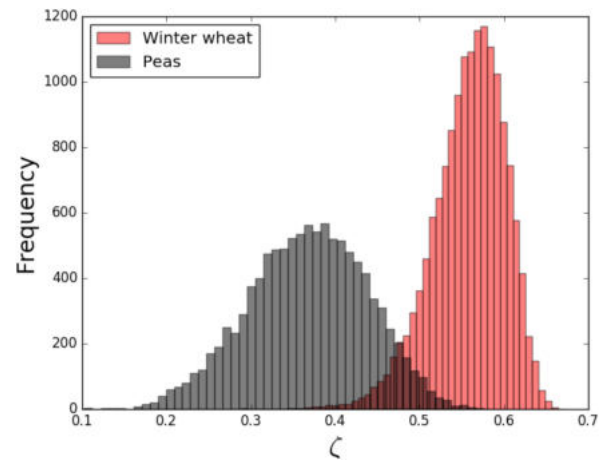

Fig. 10. Histograms of change index for winter wheat field as well as peas field [numbered "1" and "2" in Fig. 5(a) and (b), respectively].

B. Experiment II: Dual-Pol SAR—MS Modality

The Junagadh district of Gujarat can be seen, with its abundant groundnut and cotton fields, in the postmonsoon image of Sentinel 2B for October 8, 2019 [see Fig. 10(b)]. Most of the fields have fully grown groundnut or cotton and look identical in the natural color composite optical images as both fields have very similar signatures in these bands. But the growth characteristics of cotton and groundnut (groundnut being a much shorter crop even at full growth) are distinct. For CD analysis, we used premonsoon data from April 2019.

At this time, all the fields in the area shown in Fig. 10(b) are fallow (refer to Section III for a detailed exposition of data used in the experiment). ζ shows characteristics of both modalities, as seen in Fig. 11(a). Again, higher values of ζ correspond to detectable changes between the acquisitions. While waterbody shows considerably small changes, most agricultural fields show
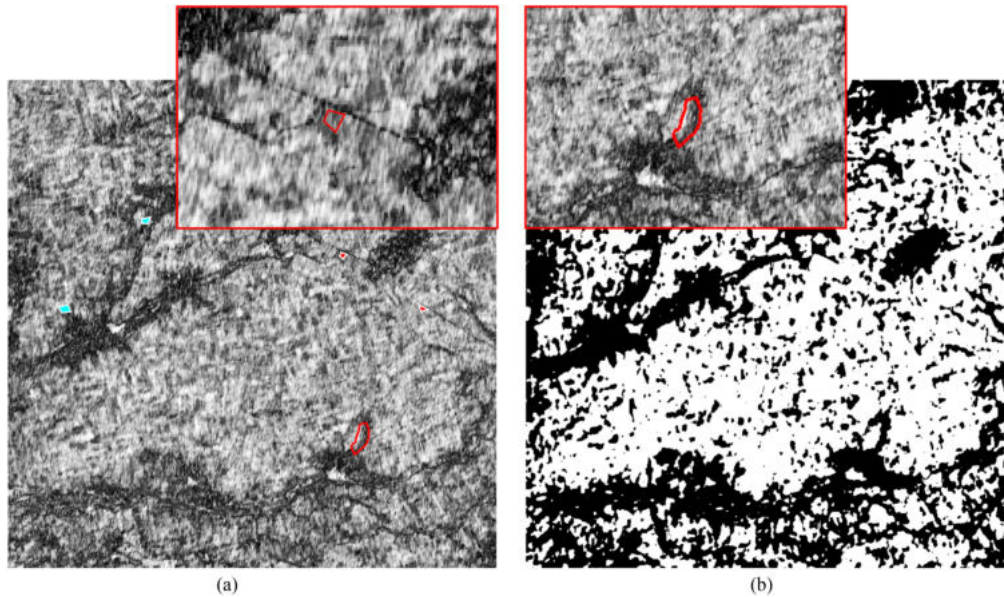
Fig. 11. (a) ζ image for the dual-pol SAR—MS fused data. The field boundaries visible in the optical data have been blurred in the process, but more information is now available for CD analysis compared to each modality taken alone. The red outline is a waterbody. The filled in red polygons are groundnut fields, and the cyan polygons are cotton fields sampled during the GT campaign. (b) Binary change image using local adaptive thresholding on ζ. (Inset) (a) Zoomed-in ζ image containing a groundnut field. (b) Zoomed-in image around the waterbody.

TABLE IV
MEDIAN AND IQR OF VARIOUS CHANGE INDICES FOR THE GROUNDNUT AND COTTON FIELDS

Index	Groundnut		Cotton	
	Median	IQR	Median	IQR
ζ	0.69	0.19	0.38	0.16
ζ_{Opt}	0.43	0.06	0.18	0.03
ζ_{SAR}	0.45	0.22	0.36	0.20
ζ_{Stack}	0.42	0.08	0.26	0.09

the change (bright areas in the ζ image). This is visible from the binary change map in Fig. 11(b).

Like in the case of dual-frequency SAR modality, the ζ index is sensitive to a different rate of crop growths and aids in discrimination between groundnut and cotton. The median value for the cotton crop is much lower (0.38 with an IQR of 0.16) as compared to that of the groundnut crop (0.69 with IQR of 0.19). Even though this is true for single-modality indices (ζ_{Opt} and ζ_{SAR}), the relative difference is higher in the new index (see Table IV). Fig. 11 also depicts cotton and groundnut fields sampled during the field survey. The red polygons represent groundnut fields, whereas the cyan ones are cotton fields. According to Fig. 12(c), the cotton crop has undergone less change as compared to the groundnut crop. However, both the fields look very similar in the optical regime (ζ consistently registers higher values for groundnut crop). We can use this to differentiate two kinds of changes via simple thresholding.

Cotton grows slower than groundnut, and the magnitude of change index also reflects the difference in the relative growth.

From the boxplots of Fig. 12, one can note that the dispersion in ζ is less while using optical bands alone as compared to SAR. This is due to less system noise in the optical imaging system than the speckle noise in coherent SAR. One should note that, due to monsoon growth, most of the agriculture pixels have changed, so our methodology of using a single ζ parameter may not be optimal for multiclass CD. However, we can utilize the extra information in the change vectors (before taking the Frobenius norm) via CVA for multiclass CD.

The sensitivity to crop growth (for the case of groundnut as well as cotton) is much higher in the proposed index as compared to either modality taken alone, as can be easily noticed from Fig. 12(c). Single modality ζ is computed using (12), just as in the previous example. The MS-only index has a lower magnitude of change than the SAR-only case (median of 0.43 with IQR of 0.06), but the crops are separable. However, SAR only ζ has overlapping boxes for cotton and groundnut, making the separability difficult (median of 0.45 but with an IQR of 0.22). As expected, the fused ζ has more robust information assimilated from both sources.

We can make a direct comparison with the stacking technique, a popular way of pixel-level fusing data from different sensors [20]. Direct stacking of bands can be used to derive ζ (without the Kronecker product). But this provides a less sensitive change index that saturates quickly. Fig. 12(b) gives the output from such a scheme, which looks very much like the change index from optical bands alone [see Fig. 12(a)]. This is why the median value of stacked ζ_{Stack} and IQR closely matches ζ_{Opt} for cotton and groundnut crops in the boxplot. It is clear from Fig. 12(c) that the optical bands or a direct stacking method registers a much lower median change for both the crops as compared to the proposed method, while crops are
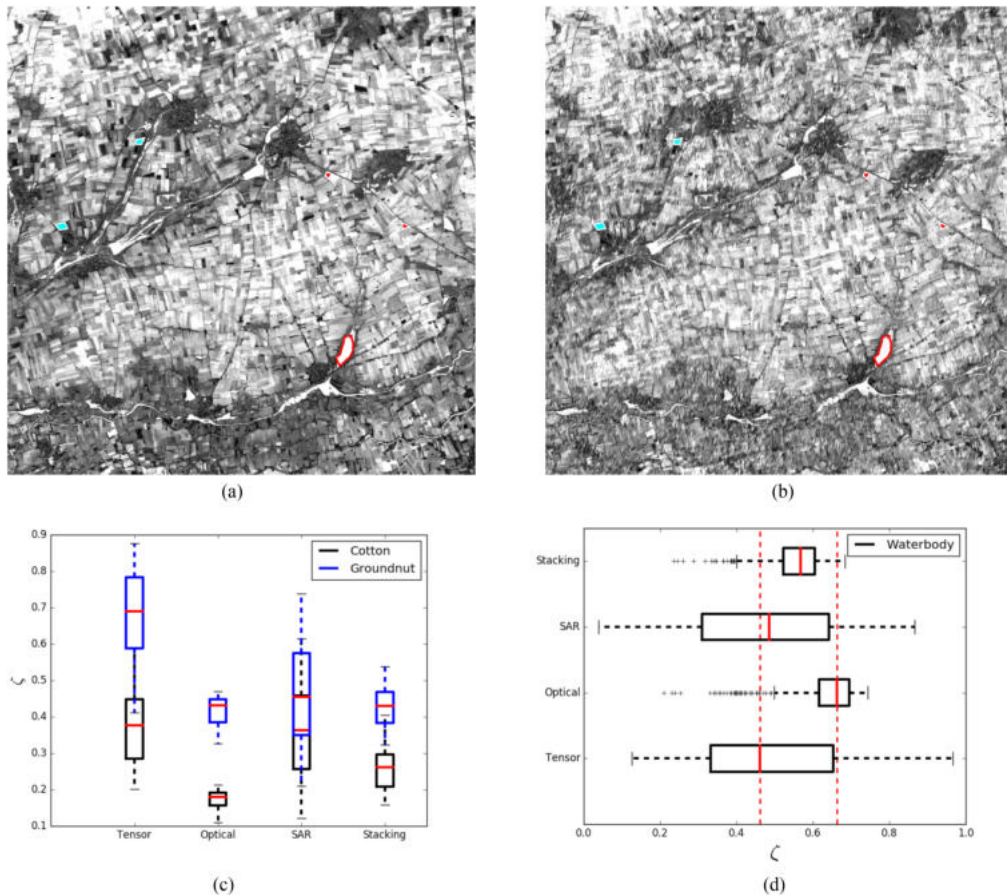
Fig. 12. (a) ζ image using only the MS bands. (b) ζ image for the dual-pol SAR—MS fused data using band stacking. This image closely resembles that of (a) despite the band stacking. (c) Box plot of the change index for a sample cotton and groundnut field (black boxes represent groundnut, whereas blue boxes represent cotton field). (d) Box plot of the change index for the marked waterbody registers sufficient change in the MS image and very little change in the SAR image.

less separable in SAR only ζ_{SAR}. The fused ζ not only registers much bigger change for both crops, but is also well separable. We have tabulated results in Table IV for quick reference.

Furthermore, direct stacking of SAR and MS bands has not brought about any new dimension to the ζ index beyond what was possible with MS bands alone. This is not the case with the proposed method. To illustrate this point, let us consider the waterbody in the image marked by the red polygon. As evident from Fig. 12(a), this feature registers drastic change between the pre- and postmonsoon MS acquisitions (as evidenced by the bright tone within the red polygon in the MS-only change index). But the change is not high in the SAR acquisitions [see the ζ_{SAR} boxplot in Fig. 12(d)]. Interestingly, the SAR-MS stacking-based ζ mimics the behavior of the MS-only index, as shown in Fig. 12(b).

Visually, the changes in water bodies are generally suppressed in the new index [the darker areas in Fig. 11(a)]. This observation is made concrete in the boxplot depicted in Fig. 12(d). The median value for the new change index (for waterbody outlined by red polygon) is much less than optical bands or stacking. The SAR-only ζ also shows lower values as the fused ζ. This directly demonstrates that the proposed method achieves a proper fusion of information available in either modality. In contrast, direct stacking of bands biases the fused data properties toward the MS bands. The widening IQR can also see the proper hybridization

of information in the fused ζ modalities compared to the MS case. This is absent again in the stacking technique.

For the 3272×4734 tiles used in the dual-pol SAR-MS fusion, the process finishes within 25 min in the python3 framework on a workstation with 64-GB RAM and Intel Xeon processor. In this experiment, we made no prior assumption about the data distribution, which we could easily extend to other RS data modalities. Combined with the simplicity of implementation, this formalism can be of great importance while tackling multimodal CD problems.

V. CONCLUSION

In this article, we proposed a general framework for CD utilizing the Kronecker product between two vectors/matrices to analyze multimodal data. The framework is sensor independent and provides results with statistical techniques specifically tailored to particular sensor data. We showcased two experiments, one with dual-frequency PolSAR data and the other with dual-pol SAR and MS data, with validation using extensive GT. We obtained the FP dual-frequency PolSAR data from the Danish airborne SAR system, EMISAR. We obtained the dual-pol SAR and the MS data from the Sentinel constellation of satellites. We showed that the proposed novel change index, ζ, adapts diverse information from L- and C-bands and correlates

better with various crops growth stages. The method also gave similar performance to that of techniques tailored explicitly to PolSAR data. We reached a similar conclusion for the dual-pol SAR and MS modality, where we performed a direct comparison with the data stacking method. All results were strongly supported by extensive GT data collected synchronously with the acquisitions. Our studies aim toward a worthwhile direction for multimodal (multifrequency, multisensor, etc.) data assimilation and CD studies. Vectorizing the Kronecker product for the CVA yields many exciting properties yet to be exploited for a multiclass CD framework.

ACKNOWLEDGMENT

REFERENCES

[1] N. Longbotham et al., "Multi-modal change detection, application to the detection of flooded areas: Outcome of the 2009–2010 data fusion contest," IEEE J. Sel. Topics Appl. Earth Observ. Remote Sens., vol. 5, no. 1, pp. 331–342, Feb. 2012.

[2] J. Zhang, "Multi-source remote sensing data fusion: Status and trends," Int. J. Image Data Fusion, vol. 1, no. 1, pp. 5–24, 2010.

[3] Y. You, J. Cao, and W. Zhou, "A survey of change detection methods based on remote sensing images for multi-source and multi-objective scenarios," Remote Sens., vol. 12, no. 15, 2020, Art. no. 2460.

[4] M. Dalla Mura, S. Prasad, F. Pacifici, P. Gamba, J. Chanussot, and J. A. Benediktsson, "Challenges and opportunities of multimodality and data fusion in remote sensing," Proc. IEEE, vol. 103, no. 9, pp. 1585–1601, Sep. 2015.

[5] C. C. Petit and E. F. Lambin, "Integration of multi-source remote sensing data for land cover change detection," Int. J. Geograph. Inf. Sci., vol. 15, no. 8, pp. 785–803, 2001.

[6] X. Miao, J. S. Heaton, S. Zheng, D. A. Charlet, and H. Liu, "Applying tree-based ensemble algorithms to the classification of ecological zones using multi-temporal multi-source remote-sensing data," Int. J. Remote Sens., vol. 33, no. 6, pp. 1823–1849, 2012.

[7] R. Shen, A. Huang, B. Li, and J. Guo, "Construction of a drought monitoring model using deep learning based on multi-source remote sensing data," Int. J. Appl. Earth Observ. Geoinf., vol. 79, pp. 48–57, 2019.

[8] A. Singh, "Review article digital change detection techniques using remotely-sensed data," Int. J. Remote Sens., vol. 10, no. 6, pp. 989–1003, 1989.

[9] L. Bruzzone and F. Bovolo, "A novel framework for the design of change-detection systems for very-high-resolution remote sensing images," Proc. IEEE, vol. 101, no. 3, pp. 609–630, Mar. 2013.

[10] D. R. Panuju, D. J. Paull, and A. L. Griffin, "Change detection techniques based on multispectral images for investigating land cover dynamics," Remote Sens., vol. 12, no. 11, 2020, Art. no. 1781.

[11] O. A. Ajadi, F. J. Meyer, and P. W. Webley, "Change detection in synthetic aperture radar images using a multiscale-driven approach," Remote Sens., vol. 8, no. 6, 2016, Art. no. 482.

[12] F. Gao, X. Liu, J. Dong, G. Zhong, and M. Jian, "Change detection in SAR images based on deep semi-NMF and SVD networks," Remote Sens., vol. 9, no. 5, 2017, Art. no. 435.

[13] K. Conradsen, A. Nielsen, J. Schou, and H. Skriver, "A test statistic in the complex Wishart distribution and its application to change detection in polarimetric SAR data," IEEE Trans. Geosci. Remote Sens., vol. 41, no. 1, pp. 4–19, Jan. 2003.

[14] J. Schou, H. Skriver, A. Nielsen, and K. Conradsen, "CFAR edge detector for polarimetric SAR images," IEEE Trans. Geosci. Remote Sens., vol. 41, no. 1, pp. 20–32, Jan. 2003.

[15] V. Akbari, S. N. Anfinsen, A. P. Doulgeris, and T. Eltoft, "The Hotelling-Lawley trace statistic for change detection in polarimetric SAR data under the complex Wishart distribution," in Proc. IEEE Int. Geosci. Remote Sens. Symp., 2013, pp. 4162–4165.

[16] V. Akbari, S. N. Anfinsen, A. P. Doulgeris, T. Eltoft, G. Moser, and S. B. Serpico, "Polarimetric SAR change detection with the complex Hotelling-Lawley trace statistic," IEEE Trans. Geosci. Remote Sens., vol. 54, no. 7, pp. 3953–3966, Jul. 2016.

[17] F. Bovolo and L. Bruzzone, "A theoretical framework for unsupervised change detection based on change vector analysis in the polar domain," IEEE Trans. Geosci. Remote Sens., vol. 45, no. 1, pp. 218–236, Jan. 2007.

[18] F. Bovolo, S. Marchesi, and L. Bruzzone, "A framework for automatic and unsupervised detection of multiple changes in multitemporal images," IEEE Trans. Geosci. Remote Sens., vol. 50, no. 6, pp. 2196–2212, Jun. 2012.

[19] D. Ratha, S. De, T. Celik, and A. Bhattacharya, "Change detection in polarimetric SAR images using a geodesic distance between scattering mechanisms," IEEE Geosci. Remote Sens. Lett., vol. 14, no. 7, pp. 1066–1070, Jul. 2017.

[20] S. Mahyoub, A. Fadil, E. M. Mansour, H. Rhinane, and F. Al-Nahmi, "Fusing of optical and synthetic aperture radar (SAR) remote sensing data: A systematic literature review (SLR)," Int. Arch. Photogrammetry, Remote Sens. Spatial Inf. Sci., vol. XLII-4/W12, pp. 127–138, 2019.

[21] G. Hong, Y. Zhang, and B. Mercer, "A wavelet and IHS integration method to fuse high resolution SAR with moderate resolution multispectral images," Photogrammetric Eng. Remote Sens., vol. 75, no. 10, pp. 1213–1223, 2009.

[22] D. K. Seo, Y. H. Kim, Y. D. Eo, M. H. Lee, and W. Y. Park, "Fusion of SAR and multispectral images using random forest regression for change detection," ISPRS Int. J. Geo-Inf., vol. 7, no. 10, 2018, Art. no. 401.

[23] H. Zhang and R. Xu, "Exploring the optimal integration levels between SAR and optical data for better urban land cover mapping in the Pearl river delta," Int. J. Appl. Earth Observ. Geoinf., vol. 64, pp. 87–95, 2018.

[24] H. McNairn, J. Shang, X. Jiao, and C. Champagne, "The contribution of ALOS PALSAR multipolarization and polarimetric data to crop classification," IEEE Trans. Geosci. Remote Sens., vol. 47, no. 12, pp. 3981–3992, Dec. 2009.

[25] H. McNairn, C. Champagne, J. Shang, D. Holmstrom, and G. Reichert, "Integration of optical and synthetic aperture radar (SAR) imagery for delivering operational annual crop inventories," ISPRS J. Photogrammetry Remote Sens., vol. 64, no. 5, pp. 434–449, 2009.

[26] C. Liao et al., "Synergistic use of multi-temporal RADARSAT-2 and VEN µ S data for crop classification based on 1D convolutional neural network," Remote Sens., vol. 12, no. 5, 2020, Art. no. 832.

[27] A. Shakya, M. Biswas, and M. Pal, "CNN-based fusion and classification of SAR and optical data," Int. J. Remote Sens., vol. 41, no. 22, pp. 8839–8861, 2020.

[28] R. Touati, M. Mignotte, and M. Dahmane, "Multimodal change detection using a convolution model-based mapping," in Proc. 9th Int. Conf. Image Process. Theory, Tools Appl., 2019, pp. 1–6.

[29] M. Mignotte, "A fractal projection and Markovian segmentation-based approach for multimodal change detection," IEEE Trans. Geosci. Remote Sens., vol. 58, no. 11, pp. 8046–8058, Nov. 2020.

[30] R. Touati, M. Mignotte, and M. Dahmane, "Change detection in heterogeneous remote sensing images based on an imaging modality-invariant MDS representation," in Proc. 25th IEEE Int. Conf. Image Process., 2018, pp. 3998–4002.

[31] M. Volpi, G. Camps-Valls, and D. Tuia, "Spectral alignment of multitemporal cross-sensor images with automated Kernel canonical correlation analysis," ISPRS J. Photogrammetry Remote Sens., vol. 107, pp. 50–63, 2015.

[32] Z.-g.Liu, G. Mercier, J. Dezert, and Q. Pan, "Change detection in heterogeneous remote sensing images based on multidimensional evidential reasoning," IEEE Geosci. Remote Sens. Lett., vol. 11, no. 1, pp. 168–172, Jan. 2014.

[33] A. A. Nielsen, K. Conradsen, and H. Skriver, "Change detection in full and dual polarization, single- and multifrequency SAR data," IEEE J. Sel. Topics Appl. Earth Observ. Remote Sens., vol. 8, no. 8, pp. 4041–4048, Aug. 2015.

[34] A. Schmitt, A. Wendleder, and S. Hinz, "The Kennaugh element framework for multi-scale, multi-polarized, multi-temporal and multi-frequency

SAR image preparation," *ISPRS J. Photogrammetry Remote Sens.*, vol. 102, pp. 122–139, 2015.

[35] M. Shimoni, D. Borghys, R. Heremans, C. Perneel, and M. Acheroy, "Fusion of PolSAR and PolinSAR data for land cover classification," *Int. J. Appl. Earth Observ. Geoinf.*, vol. 11, no. 3, pp. 169–180, 2009.

[36] P. Zhang, M. Gong, L. Su, J. Liu, and Z. Li, "Change detection based on deep feature representation and mapping transformation for multi-spatial-resolution remote sensing images," *ISPRS J. Photogrammetry Remote Sens.*, vol. 116, pp. 24–41, 2016.

[37] M. Gong, P. Zhang, L. Su, and J. Liu, "Coupled dictionary learning for change detection from multisource data," *IEEE Trans. Geosci. Remote Sens.*, vol. 54, no. 12, pp. 7077–7091, Dec. 2016.

[38] L. T. Luppino *et al.*, "Deep image translation with an affinity-based change prior for unsupervised multimodal change detection," *IEEE Trans. Geosci. Remote Sens.*, to be published, doi: 10.1109/TGRS.2021.3056196.

[39] W. Zhao, Z. Wang, M. Gong, and J. Liu, "Discriminative feature learning for unsupervised change detection in heterogeneous images based on a coupled neural network," *IEEE Trans. Geosci. Remote Sens.*, vol. 55, no. 12, pp. 7066–7080, Dec. 2017.

[40] R. Touati and M. Mignotte, "An energy-based model encoding non-local pairwise pixel interactions for multisensor change detection," *IEEE Trans. Geosci. Remote Sens.*, vol. 56, no. 2, pp. 1046–1058, Feb. 2018.

[41] X. Xu, W. Li, Q. Ran, Q. Du, L. Gao, and B. Zhang, "Multisource remote sensing data classification based on convolutional neural network," *IEEE Trans. Geosci. Remote Sens.*, vol. 56, no. 2, pp. 937–949, Feb. 2018.

[42] P. Benedetti, D. Ienco, R. Gaetano, K. Ose, R. G. Pensa, and S. Dupuy, "M^3Fusion: A deep learning architecture for multiscale multimodal multitemporal satellite data fusion," *IEEE J. Sel. Topics Appl. Earth Observ. Remote Sens.*, vol. 11, no. 12, pp. 4939–4949, Dec. 2018.

[43] D. Hong, N. Yokoya, G.-S. Xia, J. Chanussot, and X. X. Zhu, "X-ModalNet: A semi-supervised deep cross-modal network for classification of remote sensing data," *ISPRS J. Photogrammetry Remote Sens.*, vol. 167, pp. 12–23, 2020.

[44] D. Hong *et al.*, "More diverse means better: Multimodal deep learning meets remote-sensing imagery classification," *IEEE Trans. Geosci. Remote Sens.*, vol. 59, no. 5, pp. 4340–4354, May 2021.

[45] D. Hong, J. Hu, J. Yao, J. Chanussot, and X. X. Zhu, "Multimodal remote sensing benchmark datasets for land cover classification with a shared and specific feature learning model," *ISPRS J. Photogrammetry Remote Sens.*, vol. 178, pp. 68–80, 2021.

[46] P. A. Grillet, *Abstract Algebra*, 2nd ed. New York, NY, USA: Springer, 2007.

[47] N. Otsu, "A threshold selection method from gray-level histograms," *IEEE Trans. Syst., Man, Cybern.*, vol. SMC-9, no. 1, pp. 62–66, Jan. 1979.

[48] D. Bradley and G. Roth, "Adaptive thresholding using the integral image," *J. Graph. Tools*, vol. 12, no. 2, pp. 13–21, 2007.

[49] G. D. Batten, "Plant analysis using near infrared reflectance spectroscopy: The potential and the limitations," *Aust. J. Exp. Agriculture*, vol. 38, no. 7, pp. 697–706, 1998.

[50] C. Li, J. Xue, and B. Su, "Significant remote sensing vegetation indices: A review of developments and applications," *J. Sens.*, vol. 2017, pp. 1353691–1353708, 2017.

[51] E. Christensen *et al.*, "EMISAR: An absolutely calibrated polarimetric L- and C-band SAR," *IEEE Trans. Geosci. Remote Sens.*, vol. 36, no. 6, pp. 1852–1865, Nov. 1998.

[52] A. A. Nielsen, H. Skriver, and K. Conradsen, "Complex Wishart distribution based analysis of polarimetric synthetic aperture radar data," in *Int. Workshop Anal. Multi-Temporal Remote Sens. Images*, Jul. 2007, pp. 1–6, doi: 10.1109/MULTITEMP.2007.4293078.

[53] M. El Hajj, N. Baghdadi, H. Bazzi, and M. Zribi, "Penetration analysis of SAR signals in the C and L bands for wheat, maize, and grasslands," *Remote Sens.*, vol. 11, no. 1, 2019, Art. no. 31.

[54] H. Skriver, M. T. Svendsen, and A. G. Thomsen, "Multitemporal C- and L-band polarimetric signatures of crops," *IEEE Trans. Geosci. Remote Sens.*, vol. 37, no. 5, pp. 2413–2429, Sep. 1999.

[55] A. Refice, M. Zingaro, A. D' Addabbo, and M. Chini, "Integrating C- and L-band SAR imagery for detailed flood monitoring of remote vegetated areas," *Water*, vol. 12, no. 10, 2020, Art. no. 2745.

Sanid Chirakkal received the master's degree in physics from the University of Calicut, Malappuram, India, in 2009, and the Ph.D. degree in physical sciences from the Indian Institute of Space Science and Technology, Thiruvananthapuram, India, in 2014.

He was a Visiting Fellow with the Remote Sensing Laboratory, University of Trento, Trento, Italy, in 2019 as a part of India–Trento Program for Advanced Research. In 2015, he joined the Space Applications Centre, Indian Space Research Organization (ISRO), Ahmedabad, India, at the erstwhile Advanced Techniques Development Division, which is now the Microwave Techniques Development Division. After joining ISRO, he contributed significantly toward the development of an indigenous synthetic aperture radar (SAR) data processing software suite (Microwave Data Analysis Software), which received an Indian copyright. In addition, he has played a key role in developing an end-to-end python-based differential interferometric SAR processing tool for ISRO SAR missions and a polarimetric SAR interferometry (PolInSAR) module for forest height retrieval of Indian forests at the Space Applications Centre. His research interests include advanced areas of SAR, such as polarimetric SAR, interferometric SAR, and PolInSAR, as well as nonlinear dynamical systems theory and mathematical ecology.

Dr. Chirakkal received the Indian Society of Remote Sensing National Geospatial Award for the year 2020.

Francesca Bovolo (Senior Member, IEEE) received the Laurea (B.S.) and Laurea Specialistica (M.S.) degrees (*summa cum laude*) in telecommunication engineering in 2001 and 2003, respectively, and the Ph.D. degree in communication and information technologies in 2006, all from the University of Trento, Trento, Italy.

She was a Research Fellow with the University of Trento until 2013. She is currently the Founder and the Head of Remote Sensing for Digital Earth Unit, Fondazione Bruno Kessler, Trento, and a member of the Remote Sensing Laboratory, Trento. She is one of the co-investigators of the Radar for Icy Moon Exploration instrument of the European Space Agency Jupiter Icy Moons Explorer and a member of the Science Study Team of the EnVision mission to Venus. Her research interests include remote sensing image processing, multitemporal remote sensing image analysis, change detection in multispectral, hyperspectral, and synthetic aperture radar images, and very high resolution images, time-series analysis, content-based time-series retrieval, domain adaptation, and light detection and ranging and radar sounders. She conducts research on these topics within the context of several national and international projects.

Dr. Bovolo is a member of the program and scientific committee of several international conferences and workshops. She was a recipient of the First Place in the Student Prize Paper Competition of 2006 IEEE International Geoscience and Remote Sensing Symposium, Denver, CO, USA, 2006. She was the Technical Chair of the 6th International Workshop on the Analysis of Multitemporal Remote Sensing Images. She has been a Co-Chair of the SPIE International Conference on Signal and Image Processing for Remote Sensing since 2014. She was the Publication Chair of the International Geoscience and Remote Sensing Symposium in 2015. She has been an Associate Editor for the IEEE JOURNAL OF SELECTED TOPICS IN APPLIED EARTH OBSERVATIONS AND REMOTE SENSING since 2011 and the Guest Editor for the Special Issue on Analysis of Multitemporal Remote Sensing Data of IEEE TRANSACTIONS ON GEOSCIENCE AND REMOTE SENSING. She is a referee for several international journals.

Arundhati Ray Misra received the B.E. degree in electronics and communication engineering in 1984, the M.E. degree in computer science and engineering from Jadavpur University, Kolkata, India, in 1986, and the Ph.D. degree in computer science and engineering from Nirma University, Ahmedabad, India, in 2017.

Since 1986, she has been with Space Applications Center (SAC), Indian Space Research Organization (ISRO), Ahmedabad, and involved in the development of synthetic aperture radar (SAR) signal processing algorithm. She designed and developed the Processor for JPL's SEASAT (*L*-band) SAR data. She designed and developed the ERS-1 SAR processor, which was operationalized at the National Remote Sensing Centre, Hyderabad, India, in 1991. She contributed extensively to the design and development of a parallel-processor-based SAR processing algorithm, developed on the PARAM machine of the Centre for Development of Advanced Computing, Ahmedabad, which was the first indigenous Super Computer of India using multiple Transputers as the backend processors. She was designated as the Project Manager (DP) of ISRO's Multifrequency Scanning Microwave Radiometer. She was the Deputy Project Director of data products for the Joint ISRO–CNES Project, "Meghatropiques." She was involved in spaceborne millimeter-wave sounder simulation and configuration studies of spaceborne millimeter wave sounder for temperature and humidity sounding of ISRO. She was deputed as the Guest Scientist to German Aerospace Center, Germany, where she designed and developed the DInSAR processor for ESAR sensor. She is also involved in the hyperspectral technique development activities in SAC. She is also the Group Director of the Advanced Microwave and Hyperspectral Technique Development Group, SAC, ISRO. Her research interests include SAR, radiometer, scatterometer, mm-sounder, interferometric SAR, polarimetric SAR, wavelet-based studies, and hyperspectral techniques development.

Lorenzo Bruzzone (Fellow, IEEE) received the Laurea (M.S.) degree in electronic engineering (*summa cum laude*) and the Ph.D. degree in telecommunications from the University of Genoa, Genoa, Italy, in 1993 and 1998, respectively.

He is currently a Full Professor of Telecommunications with the University of Trento, Trento, Italy, where he teaches remote sensing, radar, and digital communications. He is the Founder and the Director of the Remote Sensing Laboratory, Department of Information Engineering and Computer Science, University of Trento. He is the Principal Investigator of many research projects. Among the others, he is currently the Principal Investigator of the *Radar for Icy Moon Exploration* instrument in the framework of the *Jupiter Icy Moons Explorer* mission of the European Space Agency (ESA), Paris, France, and the Science Lead for the High Resolution Land Cover project in the framework of the Climate Change Initiative of ESA. He is the author (or coauthor) of 294 scientific publications in refereed international journals (221 in IEEE journals), more than 340 papers in conference proceedings, and 22 book chapters. He is editor/co-editor of 18 books/conference proceedings and one scientific book. His papers are highly cited, as proven from the total number of citations (more than 39000) and the value of the H-index (91) (source: Google Scholar). He was invited as keynote speaker in more than 40 international conferences and workshops. He promotes and supervises research on his research interests within the frameworks of many national and international projects. His current research interests include remote sensing, radar and synthetic aperture radar (SAR), signal processing, machine learning, and pattern recognition.

Dr. Bruzzone ranked first place in the Student Prize Paper Competition of the 1998 IEEE International Geoscience and Remote Sensing Symposium, Seattle, WA, USA, July 1998. Since 2009, he has been a member of the Administrative Committee of the IEEE Geoscience and Remote Sensing Society (GRSS), where he has been the Vice-President for Professional Activities since 2019. He was the recipient of many international and national honors and awards, including the IEEE GRSS 2015 Outstanding Service Award, the 2017 and 2018 IEEE IGARSS Symposium prize paper awards, and the 2019 WHISPER Outstanding Paper Award. He was a Guest Co-Editor of many Special Issues of international journals. He is the co-founder of IEEE International Workshop on the Analysis of Multitemporal Remote-Sensing Images series and a member of the Permanent Steering Committee of this series of workshops. Since 2003, he has been the Chair of SPIE Conference on Image and Signal Processing for Remote Sensing. He is the founder of *IEEE Geoscience and Remote Sensing Magazine* for which he was the Editor-in-Chief between 2013 and 2017. He is an Associate Editor for IEEE TRANSACTIONS ON GEOSCIENCE AND REMOTE SENSING. He was the Distinguished Speaker of the IEEE Geoscience and Remote Sensing Society between 2012 and 2016.

Avik Bhattacharya (Senior Member, IEEE) received the integrated M.Sc. degree in mathematics from the Indian Institute of Technology Kharagpur, Kharagpur, India, in 2000, and the Ph.D. degree in remote sensing image processing and analysis from Télécom ParisTech, Paris, France, and the Ariana Research Group, Institut National de Recherche en Informatique et en Automatique, Nice, France, in 2007.

He is currently a Professor with the Centre of Studies in Resources Engineering, Indian Institute of Technology Bombay (IITB), Mumbai, India, where he is leading the Microwave Remote Sensing Lab. Before joining IITB, he was a Canadian Government Research Fellow with the Canadian Centre for Remote Sensing, Ottawa, ON, Canada. He received the Natural Sciences and Engineering Research Council of Canada visiting scientist fellowship at the Canadian National Laboratories from 2008 to 2011. His current research interests include synthetic aperture radar (SAR) polarimetry, statistical analysis of polarimetric SAR images, applications of radar remote sensing in agriculture, cryosphere, and urban and planetary studies.

Dr. Bhattacharya is the Editor-in-Chief for IEEE GEOSCIENCE AND REMOTE SENSING LETTERS (GRSL). He was an Associate Editor for IEEE GRSL. He was the Guest Editor for the special issue on Applied Earth Observations and Remote Sensing in India in IEEE JOURNAL OF SELECTED TOPICS IN APPLIED EARTH OBSERVATIONS AND REMOTE SENSING in 2017. He was one of the Guest Editors for the special stream on Advanced Statistical Techniques in SAR Image Processing and Analysis in IEEE GRSL in 2018. He is the Founding Chairperson of the IEEE Geoscience and Remote Sensing Society Chapter of the Bombay Section.